High-Temperature Scanning Indentation: A new method to investigate in situ metallurgical evolution along temperature ramps

Gabrielle Tiphéne, Paul Baral, Solène Comby-Dassonneville, Gaylord Guillonneau, Guillaume Kermouche, Jean-Michel Bergheau, Warren Oliver, Jean-Luc Loubet

High-Temperature Scanning Indentation: a new method to investigate in situ metallurgical evolution along temperature ramps

Authors:

Gabrielle TIPHÉNE – corresponding author

Université de Lyon, Ecole Centrale de Lyon, LTDS UMR CNRS 5513, 36 Avenue Guy de Collongue, 69134 Ecully, France

Mines Saint-Etienne, CNRS, UMR 5307 LGF, Centre SMS, F – 42023 Saint-Etienne, France.

Email: gabrielle.tiphene@ec-lyon.fr

ORCID : 0000-0001-7513-225X

Paul BARAL

Institute of Mechanics, Materials and Civil Engineering (IMMC), UCLouvain, B-1348, Louvain-la-Neuve, Belgium

Email: paul.baral@uclouvain.be

ORCID : 0000-0002-8586-0733

Solène COMBY-DASSONNEVILLE

Université de Lyon, INSA-Lyon, MATEIS UMR CNRS 5510, 7 Avenue Jean Capelle, 69621, Villeurbanne Cedex, France

Email: solene.dassonneville@insa-lyon.fr

Gaylord GUILLONNEAU

Université de Lyon, Ecole Centrale de Lyon, LTDS UMR CNRS 5513, 36 Avenue Guy de Collongue, 69134 Ecully, France

Email: gaylord.guillonneau@ec-lyon.fr

Guillaume KERMOUCHE

Mines Saint-Etienne, CNRS, UMR 5307 LGF, Centre SMS, F – 42023 Saint-Etienne, France.

Email: kermouche@emse.fr

Jean-Michel BERGHEAU

Université Lyon, Ecole Nationale d'Ingénieurs de Saint Etienne, CNRS UMR 5513 LTDS, F-42023, Saint Etienne, France

Email : jean-michel.bergheau@enise.fr

Warren OLIVER

KLA Nanomechanics Inc, Oak Ridge, USA

Email: Warren.Oliver@kla.com

Jean-Luc LOUBET

Université de Lyon, Ecole Centrale de Lyon, LTDS UMR CNRS 5513, 36 Avenue Guy de Collongue, 69134 Ecully, France

Email: Jean-Luc.Loubet@ec-lyon.fr

Keywords: nanoindentation, annealing, microstructure

Abstract

A new technique, *High-Temperature Scanning Indentation (HTSI)*, is proposed to investigate metallurgical evolution occurring during anisothermal heat treatments. This technique is based on the use of high-speed nanohardness measurements carried out during linear thermal ramping of the system with appropriate settings. A specific high-speed loading procedure, based on a quarter sinus loading function, a creep segment and a *three-steps unloading method*, permits the measurement of elastic, plastic and creep properties. The indentation cycle lasts one second to minimize thermal drift issues. This approach enables quasi-continuous measurements of elastic modulus and hardness as a function of temperature in much shorter times than previous techniques. The *HTSI* technique is validated on fused silica and pure aluminum. The application to cold-rolled aluminum undergoing thermal cycling highlights the potential of the *HTSI* technique to investigate in situ thermally activated mechanisms linked with microstructural changes such as viscoplasticity, static recovery and recrystallization mechanisms in metals. Results on aluminum were confirmed using Electron Back-Scattering Diffraction measurements.

Graphical abstract

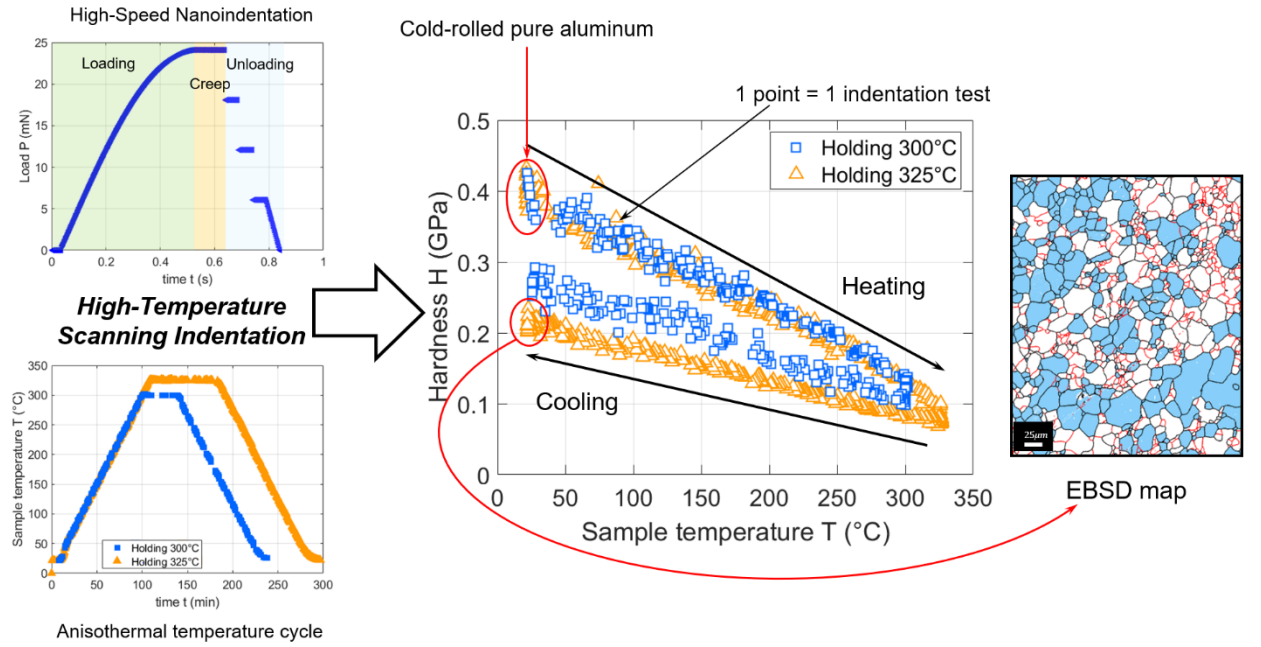

I. Introduction

Significant progress in high-temperature nanoindentation testing has been made over the last decade, opening the way to the investigation of thermally activated mechanisms at different length scales. Micron-scale measurements of the hardness, Young's modulus and even creep properties at temperatures up to 800°C and beyond now appear feasible[1–4]. A recent paper of Baral et al.[5] has also highlighted the ability of high-temperature nanoindentation to investigate in situ microstructural evolution, i.e., static recrystallization[6], in an aluminum alloy. High-temperature nanoindentation is clearly one of the most promising techniques to reveal new insights into the small-scale properties of materials.

Among all the challenges that have been overcome to allow high-temperature measurements, one of the most critical is the development of a suitable tip and sample thermal regulation to eliminate/minimize thermal drift issues[7–9]. This development has led to various regulation strategies and procedures that are usually dependent on the setup[4,7,10,11]. It is worth noting that the use of such procedures takes time[5,9,11]. Unfortunately, during such a period of time, thermally dependent physical transformations in materials can occur[12–15]. Therefore, important information can be missed. More precisely, this is a very important issue when investigating recrystallization mechanisms in polycrystalline materials[12–15] or crystallization in amorphous materials[16–22]. This issue can even affect the well-known indentation size effect, which has been deeply investigated during the past two decades[23–25]. Consequently, it is of crucial importance to develop robust nanoindentation methodologies to permit the measurement of mechanical properties at high temperature without the need to use time-consuming thermal stabilization procedures.

In the paper of Baral et al.[5], it is clearly stated that the strategy used is only relevant to characterize slow recrystallization kinetics because of both the stabilization time and the duration of an indentation test (approximately 8 min per test). The resulting lack of statistics may thus introduce an interpretation bias, mostly related to the inherent microstructure heterogeneity. Recrystallization is a thermally activated mechanism that involves nucleation of dislocation-free grains in a deformed microstructure. These nuclei grow at the extent of the former microstructure grains until the whole recrystallization process is achieved[6,26]. The dislocation-free grains are softer than the deformed grains, which allows us to discriminate them from the former grains by a simple hardness test. Therefore, the quantification of recrystallization kinetics through nanoindentation testing requires an extensive set of nanoindentation data to be independent of microstructural heterogeneity, which can be done using ultrafast indentation measurements (less than 1 s). One advantage of high-speed nanoindentation is that it should also diminish displacement drift issues. Thus, it

should even be possible to obtain data during the heating and cooling phases. Hence, the aim of this paper is to investigate whether *High Temperature Scanning Indentation*, a technique based on high-speed nanoindentation, is able to overcome the difficulties induced by the thermal stabilization time in order to pave the way for robust in situ quantifications of thermally activated physical transformations of materials.

In this paper, the first part presents the new *High Temperature Scanning Indentation* technique. A specific indentation methodology with an unloading segment, named *three-step unloading*, is proposed to avoid unloading nose issues in time-dependent materials. This technique is then validated through high-temperature experiments on fused silica and pure aluminum. The last part investigates the ability of *High Temperature Scanning Indentation* to track the mechanical properties and microstructure evolution in pure aluminum upon heating and cooling.

II. Methodology

The main objective of this paper is to conduct nonisothermal nanoindentation (i.e., during heating and cooling) to investigate in situ physical transformations in materials within a dedicated nanoindentation setup. One of the most important issues with high-temperature nanoindentation is thermal drift, which is a consequence of thermal fluctuations, mainly attributed to the tip-sample temperature mismatch. This thermal drift must remain low relative to the loading rate to ensure quantitative measurement of displacement. Therefore, specific calibration procedures must be used, depending on the temperature range and the setup. Most of the time, these calibration procedures are performed to ensure the temperature balance between the tip and the sample surface[7–9]. In this paper, the setting calibration process described by Minnert et al.[4] is used to set the temperatures of the tip in regards of the one of the sample (in isothermal conditions). The principle consists of finding the right thermal setting to minimize the displacement drift. To do so, the tip temperature is tuned during multiple tip-sample contact steps. This procedure is applied at different temperatures in the temperature range of the experiment. Once that those settings are known, the thermal ramps of the tip and the sample could be determined. When performing experiments, the tip and sample are heated using those ramps. For instance, imagine that the tip temperature should be 5°C higher than the sample at 100°C and 10°C at 200°C. Saying that the sample is heated at 3°C/min, the tip ramp should be 3.15°C/min.

This technique allows calibration of the settings for the whole thermal cycle. This procedure needs to be performed for each new tested material with a dedicated calibration sample.

1. High-speed indentation tests

To minimize the impact of the temperature variations on the displacement during heating and cooling, the indentation cycle has to be fast enough with regard to the temperature evolution during an indentation test. For instance, an increase of 0.05°C during an indentation test with a thermal ramp of 3°C/min corresponds to a test duration of 1 s.

a. Loading part

One strong interest of high-temperature indentation is the investigation of rate-dependent mechanical properties (creep). Therefore, including a holding time at constant load is appropriate here. To avoid any load overshoot at the beginning of the creep segment, it is necessary to design a loading part smoothing the transition between loading and creep segments. Clearly, the usual constant indentation strain rate segment, which is often used to satisfy the principle of geometric similarity[27,28], does not fit such a requirement. Hence, it is proposed to use a quarter sinus function instead, as illustrated in the load-versus-time curve of FIG. 1(a):

$$\mathrm{P(t)} = \mathrm{P}_{max} \sin \frac{\pi}{2t_{load}} t \qquad \text{Eq. 1}$$

where P is the load, t is the time, P_{max} is the maximum load, and t_{load} is the loading time. With such a loading procedure, the force deceleration is slow enough to permit better control of the applied force by the PID when starting the creep segment. It is worth noting that this loading function does not allow us to keep the indentation strain rate constant during the loading part. Due to device limitations, the loading time could not be faster than 0.5 s when using a quarter sinus function. However, the quarter sinus loading method can lead to artificial pop-in at the beginning of the loading part where a very high loading rate is applied at a shallow depth. This feature can be seen in FIG. 1(b) and (d) for indentation in aluminum at 300. This artifact could be avoided by defining a sigmoidal loading function for which the loading rate tends to zero at both the beginning and end of loading. Such a development is not within the scope of this paper and will be part of a complementary investigation that will deal exclusively with the analysis of pop-in during fast indentation cycles.

b. Unloading part

A quick unloading part ($\Delta t \leq 0.5\ s$) is also necessary to precisely determine the contact stiffness needed to calculate the hardness and modulus of the materials. Contrary to the loading part, there are no conditions to fulfill at the end of

the unloading part. Therefore, a linear evolution of the load with time was initially chosen as the unloading function (see FIG. 1(a)):

$$P(t) = P_{max}\left(1 - \frac{t - t_{holding}}{t_{unload}}\right) \quad \text{Eq. 2}$$

where P is the load, t is the time, P_{max} is the maximum load, t_{unload} is the time of the unloading part and $t_{holding}$ is the time at the end of the creep segment.

This method is very relevant for materials with limited time-dependent mechanical properties, such as fused silica. However, for materials that exhibit significant time-dependent mechanical properties in the investigated temperature range, such as pure aluminum at 300°C, a nose can appear on the unloading curve (see FIG. 1(b)). This feature is a well-known consequence of creep[29]. This nose is problematic regarding the fitting of the unloading curve and therefore leads to inaccurate values of the contact stiffness S, as defined by Oliver and Pharr[30]. Note that when determining the contact depth h_c (see Eq. 3 – $\frac{P_{max}}{S} \ll h_{max}$), the error in the stiffness calculation has a low impact on the contact depth determination of aluminum. In fact, unlike the elastic modulus, the hardness H is not so much impacted here, even in the presence of a nose.

Consequently, the main issue related to such a creep-induced nose is an inaccurate measurement of elastic modulus values (see Eq. 7 and Eq. 8). Ngan correction[29] was applied but did not lead to accurate stiffness measurements.

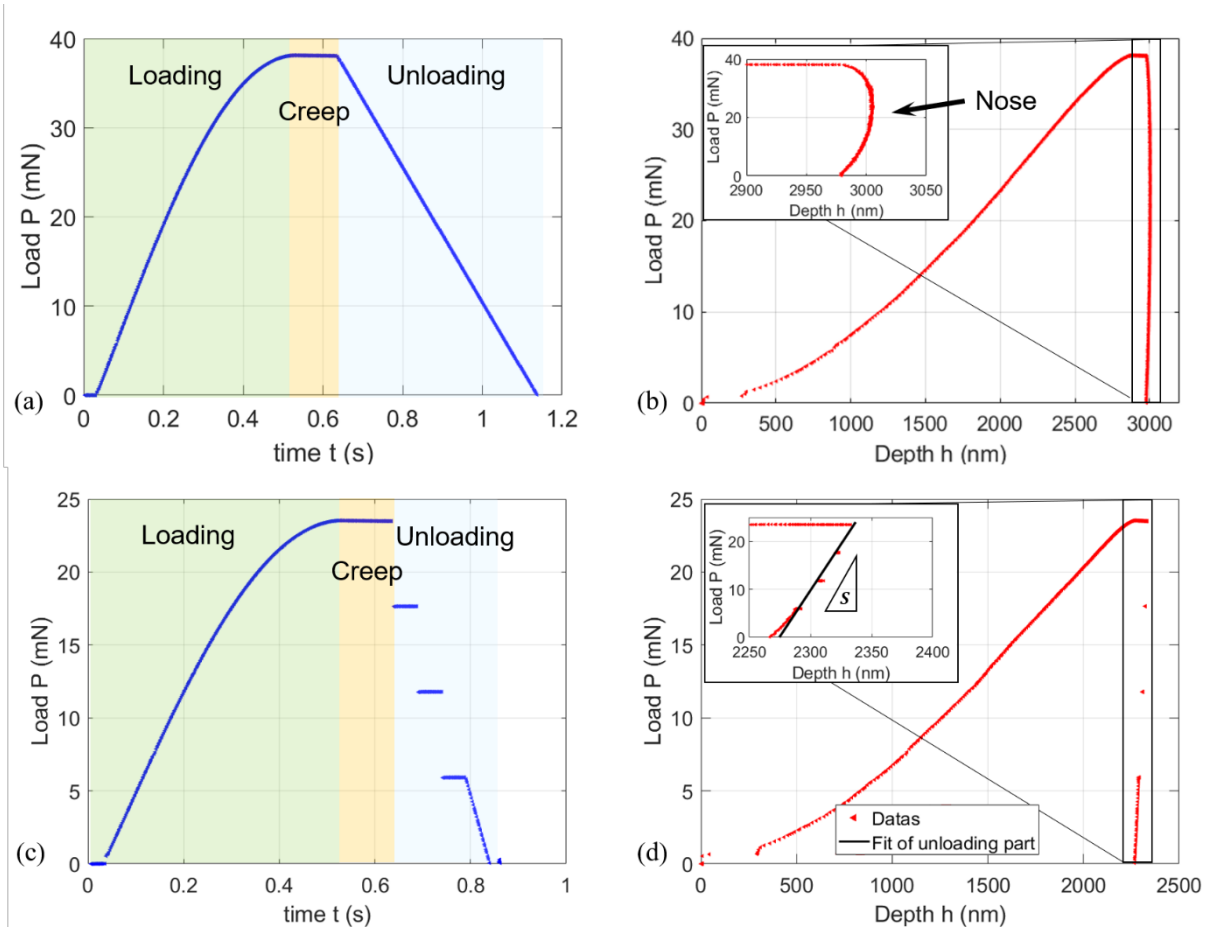

FIG. 1 (a) High-speed indentation cycle applied during initial tests. The loading part is constructed from a quarter sinus function, a holding segment is implemented to measure creep parameters, and unloading is linear over time. The whole cycle duration is less than 1.2 s. (b) Load-displacement curve measured on pure aluminum at 300°C, corresponding to the indentation cycle presented in (a). The nose on the unloading part is an issue regarding the measurement of the initial contact stiffness and thus elastic modulus. (c) Modified high-speed indentation cycle. The loading part is again constructed from a quarter sinus function, and a holding segment is implemented to measure creep parameters. Unloading is performed as quickly as possible using the three-step unloading method, i.e., three unloading steps of 0.05 s. The whole cycle lasts less than 1 s. (d) Load-displacement curve measured on pure aluminum at 300°C, corresponding to the indentation cycle presented in (c). Owing to the modified unloading procedure (i.e., the three-step unloading method), the nose is no longer observed. The unloading part can now be fitted using a linear function.

To overcome this issue, it is proposed here to use a *three-step method* during the unloading part (see FIG. 1(c)). The idea of such unloading method is to unload as fast as possible while having enough data points to accurately determine the stiffness. It is done using load steps during unloading. More precisely, a first unloading step, from P_{max} to $75\%P_{max}$, is applied instantaneously. It is stabilized for 0.05 s before decreasing to $50\%P_{max}$. The same stabilization

of 0.05 s is performed before decreasing to $25\%P_{max}$. After another 0.05 s time interval, a linear unloading part is applied. The resulting load-versus-depth curve, where the nose is no longer present, is shown in FIG. 1(d) for pure aluminum at 300°C. The unloading part of the load-displacement curve can then be fitted accurately using a linear regression with the slope corresponding to the contact stiffness S. It is worth noting that no creep occurs when the steps in load stabilize at $75\%P_{max}$, $50\%P_{max}$ or $25\%P_{max}$.

2. Methodology for data analysis

The procedure for data analysis is based on the model of Loubet[31], for which further details are given in the appendix. According to this model, the contact depth h_c is given by

$$h_c = \alpha\left(h_{max} - \frac{P_{max}}{S_u} + h_0\right) \qquad \text{Eq. 3}$$

where h_{max} and P_{max} are the maximum depth and load, respectively, at the end of the creep segment, h_0 is the tip defect and $\alpha = 1.2$ is a constant.

The unloading contact stiffness S_u is then calculated from:

$$S_u = \frac{1}{\frac{1}{S} - \frac{1}{S_{LF}}} \qquad \text{Eq. 4}$$

where S_{LF} is the load frame stiffness calibrated at the ambient environment. The load frame stiffness is supposed to remain independent of the temperature in the range of our experiments[4].

By considering the tip as perfect, the contact area A_c is given by

$$A_c = \pi \tan^2\theta \; h_c^2 \qquad \text{Eq. 5}$$

where $\theta = 70.32°$, the equivalent conical angle for a Berkovich tip.

The hardness $H\ (GPa)$ and reduced elastic modulus $E_R\ (GPa)$ are given by:

$$H = \frac{P_{max}}{A_c} \qquad \text{Eq. 6}$$

$$E_R = \frac{S_u}{2}\sqrt{\frac{\pi}{A_c}} \qquad \text{Eq. 7}$$

Finally, Young's modulus $E\ (GPa)$ is computed through:

$$E = \frac{1-\nu^2}{\frac{1}{E_R} - \frac{1-\nu_{tip}^2}{E_{tip}}} \quad \text{Eq. 8}$$

knowing the Poisson ratio of the sample ν and the tip elastic constants E_{tip} and ν_{tip}. Creep data are analyzed using the methodology presented by Baral et al.[32]. In uniaxial tests, the representative stress σ_r could be related to the representative strain rate $\dot{\varepsilon}_r$ using a power-law relation:

$$\dot{\varepsilon}_r = c\sigma_r^{1/m} \quad \text{Eq. 9}$$

where c is the strength coefficient and m is the strain rate sensitivity, which are material constants.

To relate the representative strain rate from uniaxial tests $\dot{\varepsilon}_r$ to the indentation strain rate $\dot{\varepsilon}_{ind} = \dot{h}/h$, the following expression is used, as proposed by Baral et al.[32]:

$$\dot{\varepsilon}_r = 0.44 \cot\theta \exp\left(\frac{0.2}{m}\right)\frac{\dot{h}}{h} \quad \text{Eq. 10}$$

From the same way, σ_r the representative stress is related to the hardness H:

$$\sigma_r = \frac{H}{\gamma} \quad \text{Eq. 11}$$

where γ is the constraint factor, defined by Kermouche et al.[33]:

$$\gamma = \frac{\xi_1 \cot\theta - (1-\xi_2)H/E}{\xi_3 \cot\theta} \quad \text{Eq. 12}$$

with the geometrical constants for a cone of half-induced angle $\theta = 70.32°$, i.e., Berkovich indenter, $\xi_1 = 0.66$, $\xi_2 = 0.216$ and $\xi_3 = 0.24$.

Using Eq. 9 to Eq. 12, strength coefficient c and strain rate sensitivity m are determined through a linear fit of the plot $\ln \dot{h}/h$ -$\ln \sigma_r$.

The analysis of Sherby and Armstrong[34] is used to determine the apparent activation energy Q:

$$\frac{H}{E} = C_0 \exp\frac{Q}{nRT} \quad \text{Eq. 13}$$

where C_0 is a pre-exponential constant, R is the gas constant, and n is the stress exponent, which is equal to 5 for consistency with previous studies[42].

III. Validation

The *High Temperature Scanning Indentation* technique was validated on fused silica and pure aluminum. The proposed indentation method with the *3-step unloading* part was carried out during anisothermal high-temperature cycles.

1. Validation on fused silica

The Young's modulus and hardness of fused silica versus temperature are plotted in FIG. 2. The Young's modulus of fused silica was investigated by numerous authors[11,35–40] and is known to increase with temperature. The evolution of the Young's modulus during the heating phase is in excellent agreement with the model of Spinner et al.[37]. However, the obtained hardness values are slightly lower than those from Schuh et al.[40], but they remain correct when considering possible error sources during high-temperature nanoindentation (thermal drift, tip area function changes, load frame stiffness being a function of temperature, etc.) .

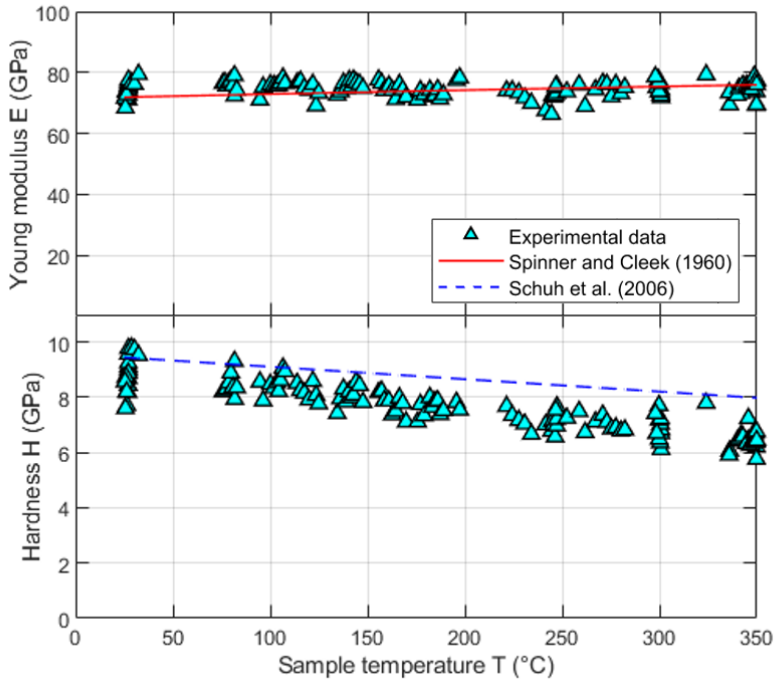

FIG. 2 Young's modulus and hardness versus temperature on fused silica during a slow thermal ramp (3°C/min). The Young's modulus values are in good agreement with the model of Spinner et al. [37]. The hardness values are also in quite good agreement compared to those of Schuh et al. [40]

2. Validation on aluminum up to 325°C

As shown in FIG. 3, the Young's modulus of aluminum decreases linearly with temperature. The trend is in agreement with the literature data[41], even if the values are slightly lower. This difference may arise from the model used for data analysis or from the assumption of constant load frame stiffness in temperature.

The hardness also decreases linearly with temperature, and the values are in agreement with literature data[42,43]. It is worth noting that care should be taken here when compared with the results of Wheeler et al. since these results are contact model dependent.

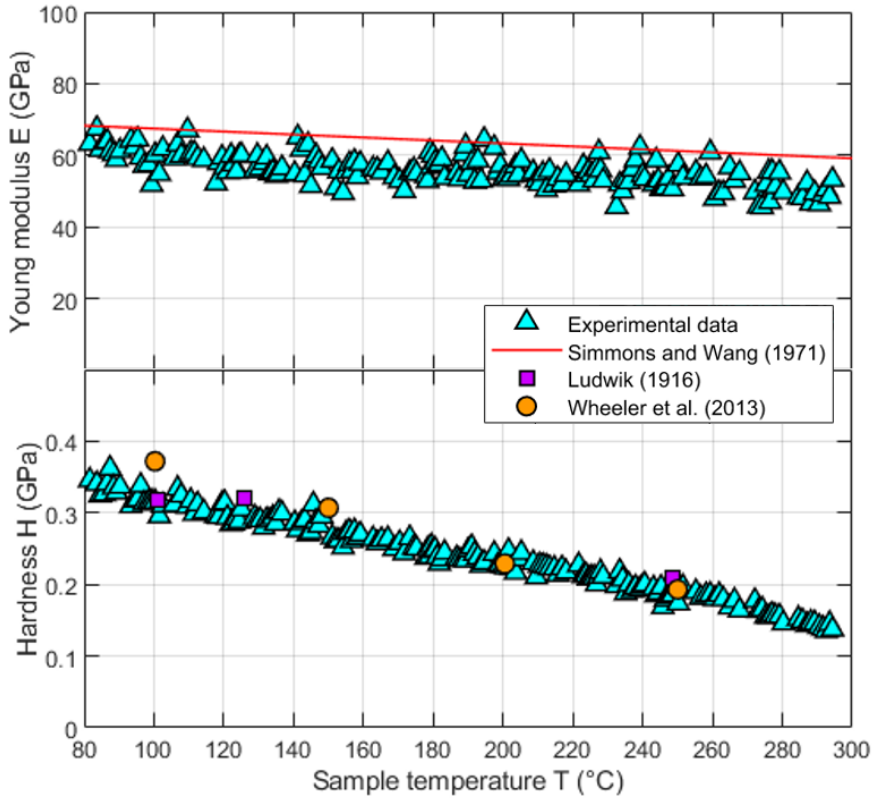

FIG. 3 Young's modulus and hardness versus temperature on pure aluminum during a slow thermal ramp (3°C/min). The reference data are from[41] for the Young's modulus and from[42,43] for hardness.

The apparent activation energy was then determined by studying the evolution of the modulus-compensated hardness H/E against T_m/T, where T is the absolute testing temperature and T_m is the absolute melting temperature (see FIG. 4 and Eq. 13). Young's modulus data in temperature were taken from[41]. Another approach would be to fit the obtained

Young's modulus data on all the interesting temperature scale to use them. However, it does not impact the following results. H/E decreases as the temperature increases. The slope of the curve gives the apparent activation energy and changes two times (at approximately $125°C$ and $250°C$). The values are consistent with the reference data[43].

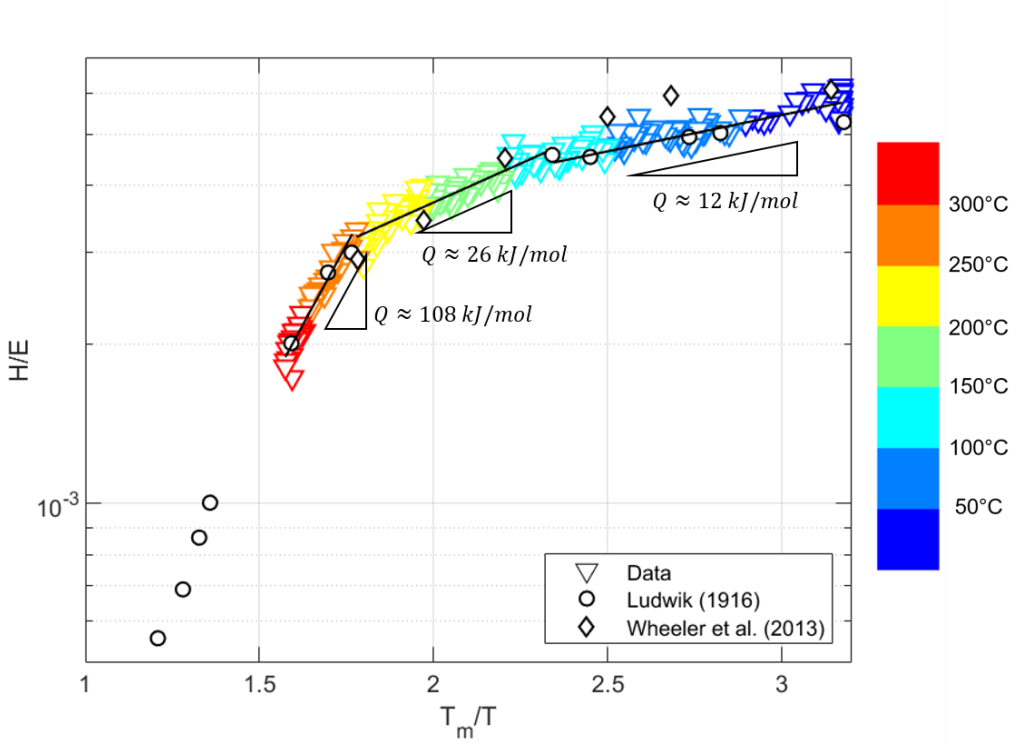

FIG. 4 Modulus-compensated hardness versus the inverse of temperature over melting temperature. The literature data are from [42,43].

The temperature-compensated indentation strain rate versus modulus-compensated hardness is plotted in FIG. 5 for an activation energy Q=130 kJ/mol. The data are close to those obtained in the literature by Phani and Oliver[44] for an activation energy Q=142 kJ/mol. Let us, however, pay attention to the fact that the contact models used to analyze the data are different. Phani and Oliver used Oliver and Pharr's model, whereas Loubet's model was used here.

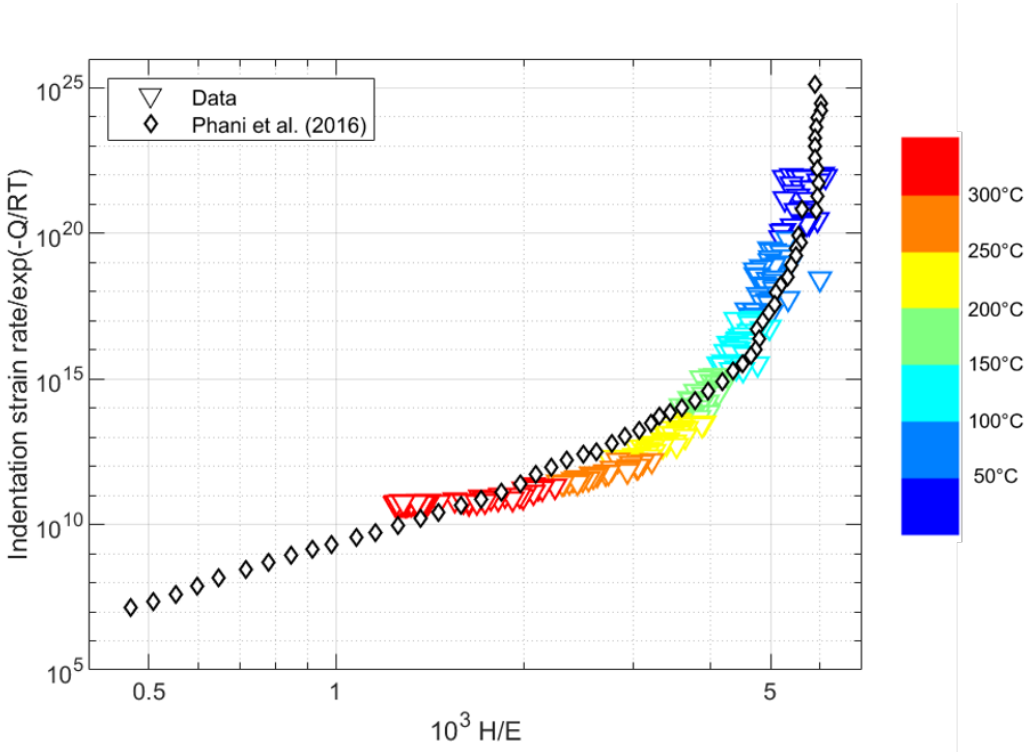

FIG. 5 Temperature-compensated indentation strain rate versus modulus-compensated hardness. The apparent activation energy is equal to $130\ kJ/mol$*. The literature data come from Phani and Oliver*[44].

In conclusion, the proposed *High Temperature Scanning Indentation* technique allows quick and precise indentation measurements to be performed during a nonisotherm thermal cycle with a quasi-continuous resolution in temperature (i.e., one data point per 1°C). By comparison with literature models and experimental data, strong validation has been performed on fused silica and aluminum for the hardness and modulus, as well as for the activation energy.

IV. Application of *High Temperature Scanning Indentation* to the monitoring of thermally activated mechanisms

1. Results

The proposed *High Temperature Scanning Indentation* technique is applied to study the in situ evolution of the mechanical properties of pure aluminum during nonisothermal temperature cycles (heating at 3°C/min, holding at 300°C or 325°C before cooling at 3°C/min). Further details on the material and thermal cycles are given in the Materials and methods section. Hardness versus temperature curves are plotted in FIG. 6(a) and (b) for the two investigated

thermal cycles. The results are well reproducible during the heating phase. The hardness appears to decrease linearly with temperature. However, a slight change in the slope can be noticed for a temperature of approximately 250°C. For both samples, a decrease in hardness occurs during the hold temperature step. During the cooling phase, the hardness increases linearly. The hardness versus temperature curves during the cooling phase are not superimposed. As shown in FIG. 9, the temperature holding segment was prescribed to occur at a higher temperature for the second experiment (holding at 325°C). Therefore, the hardness at the beginning of the cooling step for the second experiment was expected to be lower than that with the first experiment (holding at 300°C). However, the slope appears to be relatively similar. It is worth noting that this slope (in absolute value) is lower than that observed during the heating phase.

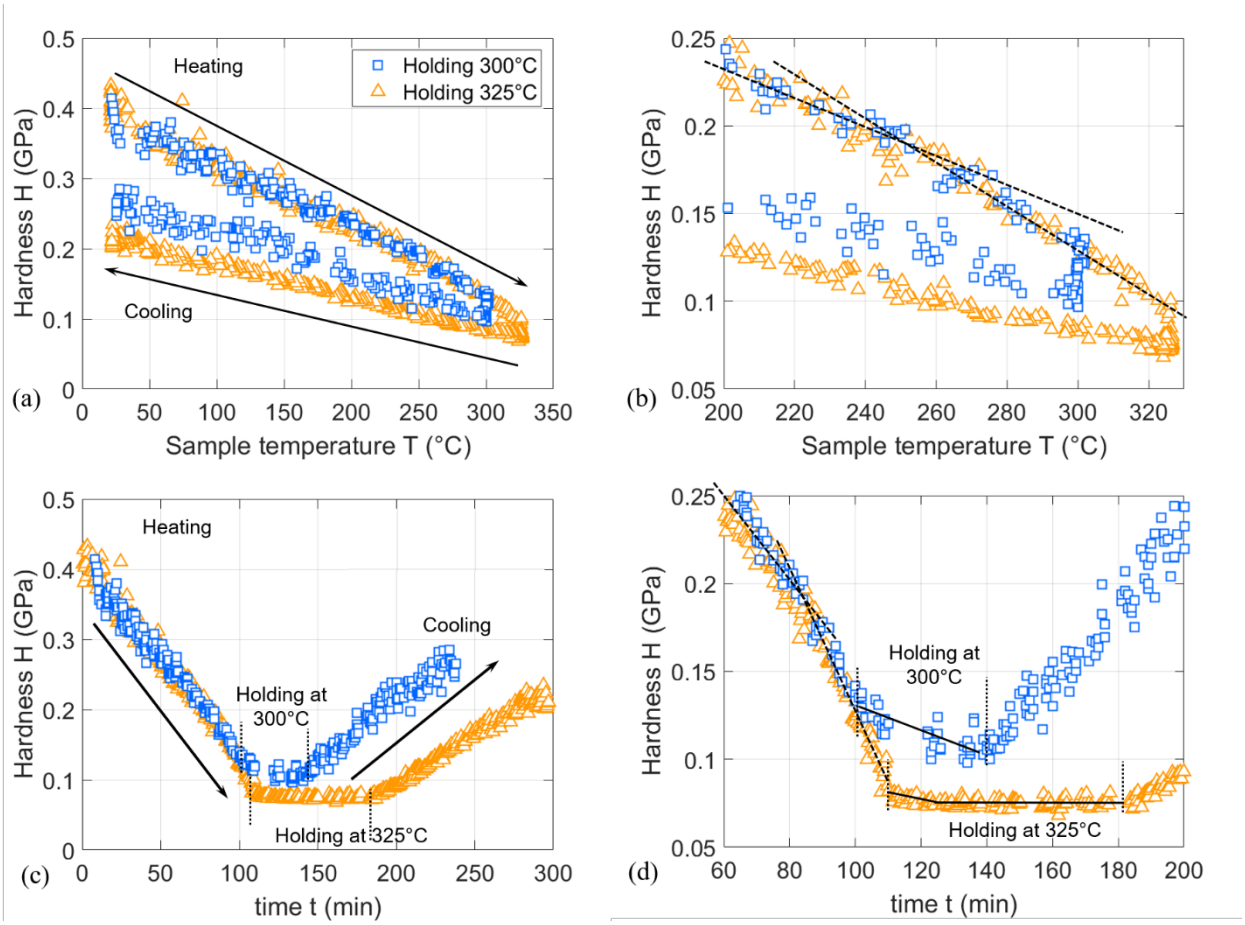

FIG. 6 (a) and (b): Hardness versus temperature for tested aluminum samples during the thermal cycles previously described, (a) during the whole thermal cycle, (b) magnified view of T>200°C. The hardness clearly changes considerably between the heating and cooling phases. The dashed lines underline the slope change during the heating phase. (c) and (d): Hardness versus time for tested aluminum samples during the thermal cycles previously described ((c) whole cycle, (d) zoom during holding phases). A

hardness decrease is observed during the hold temperature segment that may be considered a signature of recrystallization. The same change in slope during heating can be seen (dashed line).

FIG. 6(c) and (d) shows the hardness evolution versus time for the two thermal cycles. A decrease in hardness is clearly visible during the temperature holding step. It is much more pronounced for the first thermal cycle. When the sample was held at 325°C, there was a decrease during the first few minutes until the hardness stabilized.

The variation in the strain rate sensitivity m with temperature is given in FIG. 7 for the 300°C thermal cycle. Similar results are obtained for the 325°C thermal cycle. Unlike hardness, there is almost no difference between heating and cooling, even though a slightly lower value might be noticed for the cooling phase.

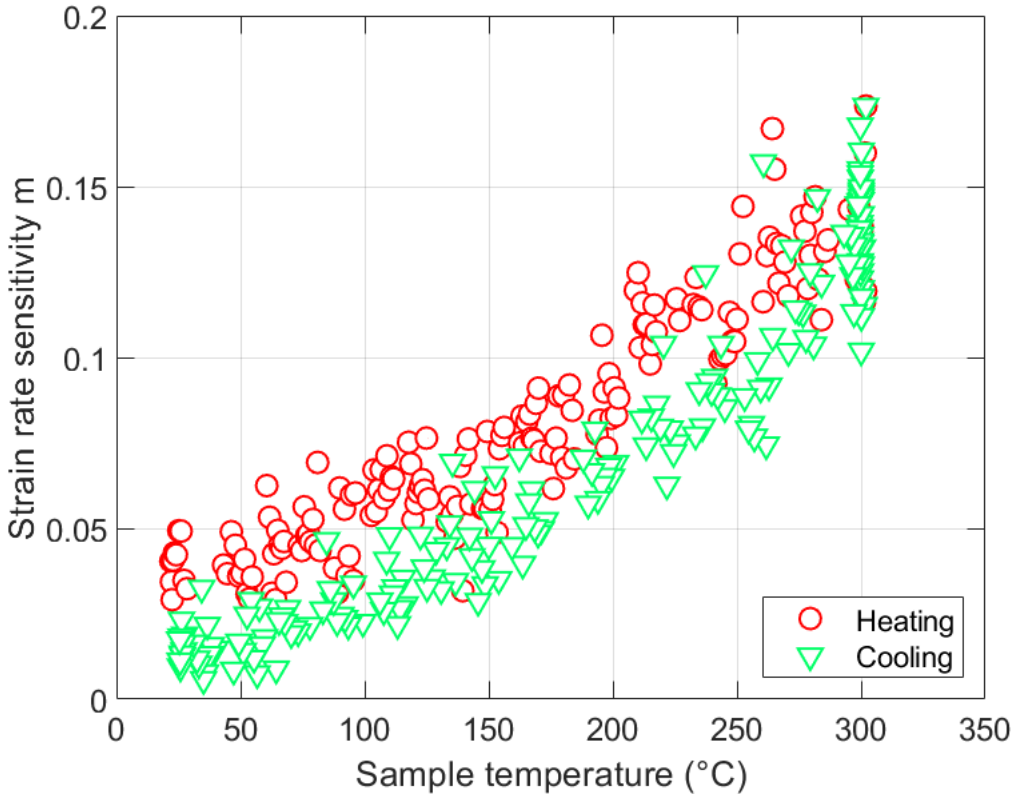

FIG. 7 Strain rate sensitivity m of an aluminum sample versus temperature during the first thermal cycle previously described.

The microstructures after thermal cycling of the two tested samples were investigated by Electron Back Scattering Diffraction (EBSD). The results are shown in FIG. 8. The black lines indicate High Angle Boundaries (HABs), misorientation angle $\theta > 15°$, and are usually considered grain boundaries. The red lines indicate Low Angle

Boundaries (LABs), $2° < \theta < 15°$, and are usually defined as subgrain boundaries. Recrystallized grains are defined as grains where the average misorientation angle θ over the grain is lower than 2°; they are colored in blue in FIG. 8.

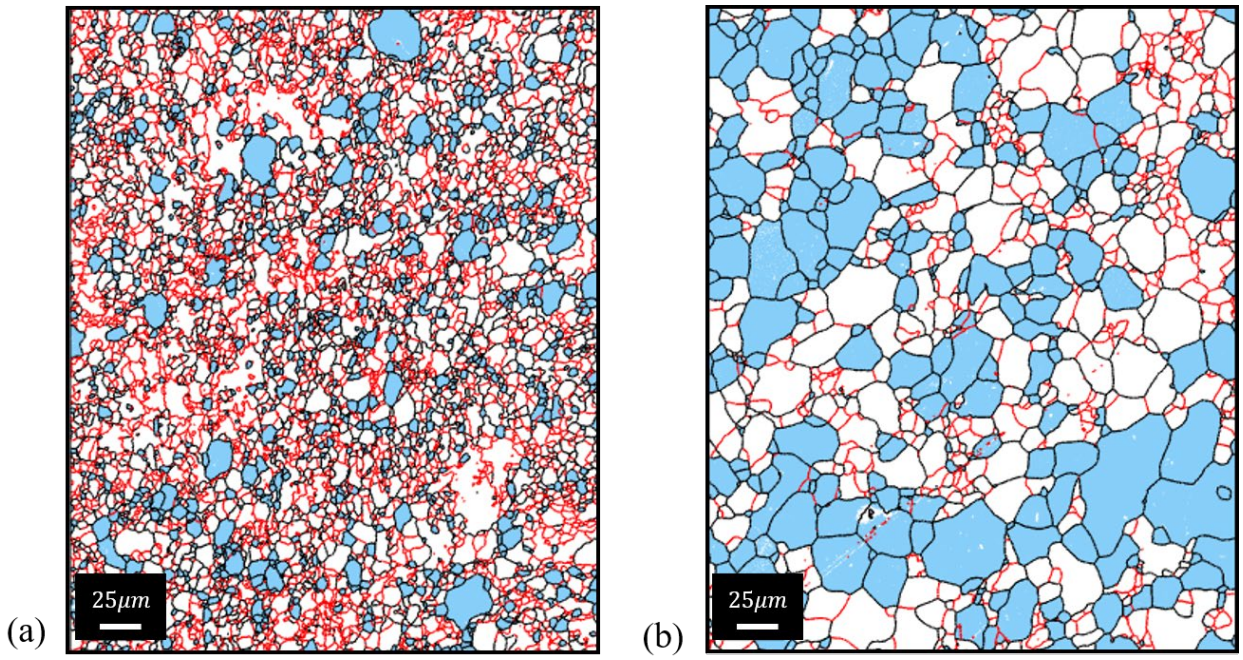

FIG. 8 Microstructure of the two studied aluminum samples after thermal cycles (a) up to 300°C and (b) up to 325°C, obtained by EBSD measurements. The grain boundaries are in black, the subgrain boundaries are in red, and the recrystallized grains are in blue. The two samples were partly recrystallized during the thermal cycles applied.

Some recrystallized grains are clearly visible on the sample heated up to 300°C. Initial grains can be identified through the presence of LABs. The recrystallization fraction is approximately 20%. In comparison, the recrystallization process was much more advanced on the sample heated up to 325°C. There are many fewer subgrain boundaries, and the recrystallized grains are relatively larger. The recrystallization fraction is closer to 50% for this thermal cycle, which is consistent with a lower hardness after the 325°C thermal cycle.

2. Discussion

The temperature dependence of the hardness can be explained through various mechanisms. Thermal activation of viscoplasticity mechanisms (activation of dislocation movements: dislocation glide, dislocation climb, etc.) that have been extensively studied for aluminum[42,45] are clearly the most important mechanisms, as pointed out in the previous

section. Nonetheless, the differences observed between heating and cooling require the consideration of other mechanisms such as static recovery and recrystallization.

The hardness of metals is known to depend upon the dislocation density[46,47]. The higher the dislocation density is, the higher the hardness. Cold work increases the amount of dislocations in metals; aluminum hardness is thus dependent on the amount of cold work. When the temperature increases, dislocation annihilation is eased due to dislocation climb and cross-slip (thermally activated viscoplasticity mechanisms), which lead to a decrease in the dislocation density (i.e., hardness). This mechanism is known as static recovery[6].

A change in the slope of the curves of hardness versus temperature (heating) – see FIG. 6 – is observed at approximately 250°C. This result might be attributed to a change in the static recovery mechanism or to the occurrence of a second metallurgical mechanism, i.e., recrystallization[6]. Such variation is also observed in FIG. 4: the apparent activation energy increases drastically at 250°C.

Recrystallization[6] is characterized by the birth and growth of new grains at the extent of the initial microstructure. The driving force of this mechanism is the stored energy (i.e., dislocation density). Recrystallized grains are characterized by a low dislocation density that is often considered null. Therefore, the hardness of recrystallized grains is significantly lower than that of a cold-rolled microstructure. So, during heating, because static recovery and recrystallization occur, the dislocation density decreases drastically, as does the hardness.

When recrystallization starts, a strong increase in the hardness standard deviation might be expected since some grains are recrystallized and other grains are not. In the current work, the volume affected by indentation is larger than the recrystallized grain size. The maximum penetration depth is approximately 3 μm (ranging from 1 μm to 3 μm depending on the temperature and recrystallization state), which corresponds to an average contact radius of 10 μm. Considering that the length of the indentation-affected volume is approximately 3 times the contact radius, it leads to a value of 30 μm when the average recrystallized grain size is approximately 5 μm (extracted from FIG. 8 for the 300°C thermal cycle). Consequently, the hardness value can be assumed to be the mixed value of the recrystallized grain and the recovered grain hardness through the recrystallization fraction. The increase in the recrystallization fraction leads to a global hardness decrease. This approach is the usual way to measure recrystallization kinetics through hardness measurements[48], even though it neglects the effects of static recovery that also influence hardness. Note that such a methodology has been applied previously in the framework of in situ high-temperature

nanoindentation by Baral et al[5]. The decrease in hardness during the hold temperature segment might be seen as the signature of recrystallization despite ongoing competition with static recovery. FIG. 8 indicates that for the sample heated to 325°C, the recrystallization fraction is much higher, which is in agreement with the thermal activation of recrystallization mechanisms. It can also be observed that the density of subgrain boundaries (i.e., dislocation density) is much lower, which means that static recovery continues parallel to recrystallization.

At the end of the high-temperature holding phase, the microstructure of the samples changed. In recrystallized grains, the density of dislocations is low compared to that of the cold-rolled sample. Therefore, during cooling, the decrease in hardness with temperature is expected to be much lower. Indeed, the temperature dependence of hardness would be mainly governed by thermal activation of viscoplasticity (in contrast to cold-rolled grains). Recovery and recrystallization become negligible.

When studying FIG. 6, hardness' decrease during holding at 300°C is higher than during holding at 325°C. However, the reverse effect would be expected since recovery and recrystallisation kinetics increases with increasing temperature. In fact, those phenomena are temperature and time-dependent. The microstructural evolution (linked to hardness variations) is the same for the two cycles up to 300°C. From this point, while the sample 1 is hold at 300°C, a linear increase of temperature (3°C/min up to 325°C) is performed. This sample experiences recovery and recrystallisation during the 8min needed to increase temperature up to 325 °C, which leads to significant hardness decrease. When starting the holding period at 325°C, recrystallisation of this sample is almost achieved: hardness will not change a lot.

It must be noted that strain rate at the end of loading is not constant as a function of temperature. This could impact the measured hardness values[49]. However, aluminum has a relatively low strain rate sensitivity, as shown in Fig. 7. When doing the experiments, an increase of strain rate at the end of the holding segment is evidenced when increasing temperature: it goes from 0.05 s^{-1} at the ambient to 0.2 s^{-1} at 325°C. To quantify the impact of such an increase on hardness values, strain rate sensitivity could be linked to hardness using [43]:

$$m = \frac{\partial \ln(H)}{\partial \ln(\dot{\epsilon})} \qquad \text{Eq. 14}$$

Saying that

$$\Delta \ln(H) = m\Delta \ln(\dot{\varepsilon}) \qquad \text{Eq. 15}$$

the impact of strain rate variation on hardness could be estimated.

The increase of strain-rate with temperature (from $0.05s^{-1}$ at 25°C to $0.2s^{-1}$ at 300°C) should induce an increase of 7% to 23% of hardness (m=0.05-0.15 – see FIG. 7). However, a decrease in hardness is observed during the tests (due to viscoplasticity, static recovery and recrystallization). The decrease that is observed would be a little higher if the measurement were carried out at the exact same strain rate for all the tested temperatures

Regarding the recrystallization mechanism, Baral et al.[5] proposed taking advantage of pop-in phenomena that are more likely on recrystallized grains than on deformed grains. Unfortunately, an artifact is observed on the load-displacement curve due to the quarter of the sinus load segment (see FIG. 1). One way to solve the problem without changing the loading function would be to use a spherical tip to postpone the load needed for the appearance of the first pop-in. However, this approach would introduce another bias in hardness evolution interpretation since self-similarity would be intrinsically lost with such a geometry.

It is clearly demonstrated here that the *High Temperature Scanning Indentation* technique, based on high-speed nanoindentation during thermal cycles, should allow the investigation of microstructural evolution mechanisms and viscoplasticity. The design of a set of experiments might be envisioned to access a limited number of experiments on the physical parameters governing viscoplasticity, recovery and recrystallization in metals in relation to the initial microstructural state.

Conclusion

This paper presents the *High Temperature Scanning Indentation* technique, a nanoindentation methodology, to track the evolution of in situ mechanical properties during a ramp of a tempering profile. The main points are as follows:

- Thermal drift issues are overcome through the use of high-speed nanoindentation;
- The loading profile using a quarter sinus segment allows measurements of hardness and creep properties;
- The Young's modulus can be measured owing to the use of the *three-step unloading method*, a specific unloading profile that limits the occurrence of an unloading nose (for time-dependent materials);
- The hardness, Young's modulus and creep properties can now be measured quasi-continuously as a function of temperature (i.e., one data point per 1°C);
- The methodology is validated on fused silica and aluminum.

This *High Temperature Scanning Indentation* methodology has been applied to cold-rolled pure aluminum that undergoes recrystallization during the tempering ramp:

- During heating, the hardness measured on similar samples is well reproducible;
- Hardness upon heating and cooling varies in a different manner, pointing out the occurrence of static recovery upon heating;
- A hardness drop is observed during the constant temperature segment. This effect is related to recrystallization, which has been assessed by postmortem EBSD microstructural characterizations;
- Creep, recovery and recrystallization mechanisms can be measured through high-speed nanoindentation testing using a suitable tempering ramp.

The nanoindentation methodology developed in this paper should allow the design of a set of experiments to measure thermally activated physical transformations in metals in a cost- and time-effective way.

Materials and methods

Materials

To validate the developed *High Temperature Scanning Indentation* technique, experiments were carried out on different materials. The validation process was started on a fused silica sample of 2 mm thickness and 12.5 mm diameter, provided by Edmund Optics. This material was chosen as a reference material for nanoindentation measurement. Its temperature properties are also well known[10,11,35–40,50].

In the second part of the validation process, two samples of pure aluminum are studied. They were also used to investigate the microstructure evolution of pure aluminum upon heating and cooling. Samples are cold laminated with a reduction of 80% of their thickness. They are 3 mm thick and 11.5 mm in diameter. These samples are mechanically polished by hand up to 1 µm (diamond solution). After indentation measurements, the two samples were electropolished to characterize the microstructural state using Electron Back-Scattering Diffraction in a JEOL FEG 6500F Scanning Electron Microscope. Postprocessing was performed using the MTEX MATLAB ToolBox[51]. The step size was set between 0.36 µm and 0.4 µm to obtain an indexation higher than 80%.

Experimental apparatus

The indentation measurements were performed using an InSEM HT nanoindentation system (KLA Nanomechanics). A doped diamond Berkovich tip was set up on the apparatus. Tip calibration was performed at ambient conditions on fused silica. Because the stiffness of the indenter is approximately $5\ 10^5 - 1\ 10^6 N/m$, when testing aluminum, the load frame stiffness was calibrated on the aluminum samples at ambient conditions prior to experiments[52]. Note that indents in aluminum are higher and deeper than in fused silica, so indentation in aluminum is very stiff compared to indentation in fused silica.

Samples were mounted the same way as in Minnert et al.[4]. All indentation tests were performed under vacuum ($< 9\ 10^{-3} Pa$), and the nanoindentation system was installed in a SEM VEGA3 system (Tescan). The distance between each indents was at least $10h_c$ [53]. The acquisition frequency was 1 kHz.

The tip and the sample were heated apart by conduction, and the heating process was controlled by specific PID loops. The settings were calibrated using the procedure presented in Section II.

Thermal cycles

On fused silica, the heating ramp was set at 3°C/min up to 350°C. On aluminum samples, the heating and cooling rates were also at 3°C/min. The holding temperatures were 300°C for 35 min and 325°C for 70 min (see FIG. 9). The cycle with holding at 325°C was used for the validation process of the new proposed methodology. On the thermal cycle with holding at 300°C, the performed indentation cycle was that with the linear unloading part (see FIG. 1(a)).

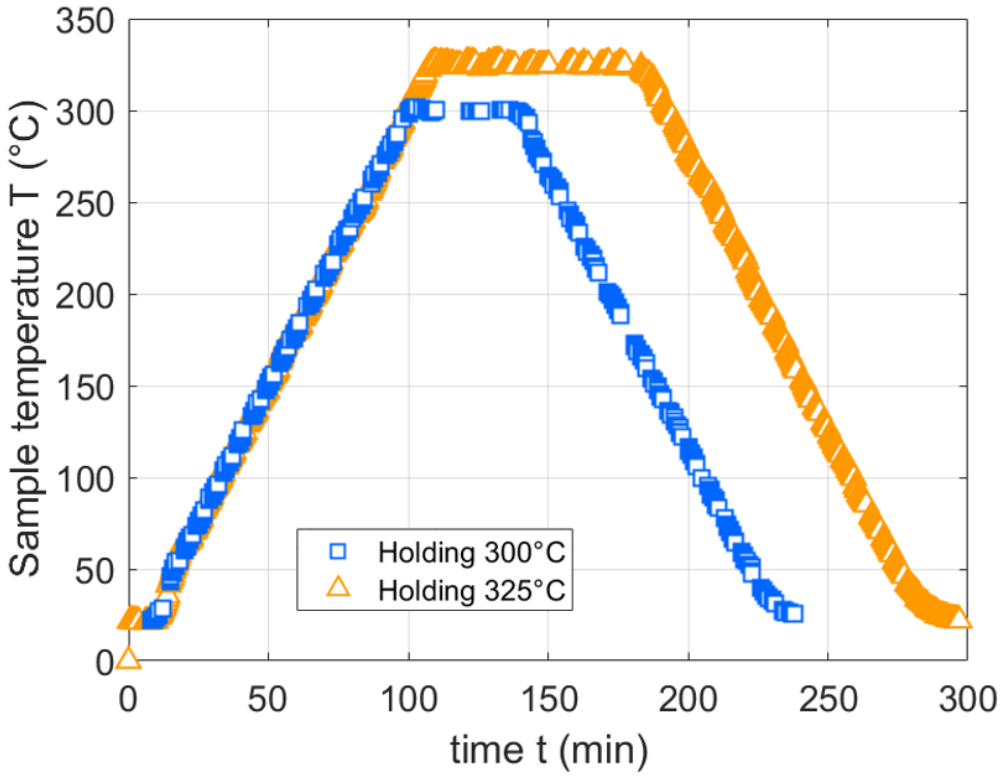

FIG. 9 Temperature versus time during two thermal cycles on pure aluminum samples: one of the aluminum samples was heated to 300°C at 3°C/min and held for 35 min before being cooled to ambient conditions (first cycle). The other was heated to 325°C at 3°C/min and held for 70 min before being cooled to ambient conditions (second cycle).

Declarations

Funding

The authors acknowledge support from the CPER MANUTECH which financed the experimental system. This work was supported by the French National Research Agency (ANR) under contract ANR-20-CE08-0022

Competing Interest

On behalf of all authors, the corresponding author states that there is no conflict of interest.

Availability of data and material

The datasets generated during and/or analyzed during the current study are available from the corresponding author on reasonable request.

Code availability

Not applicable

Appendix – The model of Loubet

1. Contact depth h_c versus contact area relation

The hardness of a material is defined as the ratio of the applied load P divided by the projected contact area A_c (see Eq. 6).

The contact area can be geometrically determined from the contact depth. For a perfect conical indenter,

$$A_c = C_0 {h_c}^2 \qquad \text{Eq. 16}$$

With C_0 a geometrical constant. For a Berkovich indenter, $C_0 = 24.56$. However, the contact depth is not directly measured and has to be calculated from the tip displacement measurement. This measurement does not account for pile-up or sink-in phenomena.

2. Plastic depth h_r'

Loubet's model is based on indentation measurements made on an elastic, perfectly plastic material. More specifically, he considers that the depth underneath the tip is purely plastic. Consequently, he relates the indentation depth to a plastic depth, named h_r', with the following expression:

$$h_r' = h - \frac{P}{S} \qquad \text{Eq. 17}$$

The plastic depth is presented in FIG. 10 and FIG. 11. FIG. 11 shows the intersection between the displacement axis and the linear fit with the S slope.

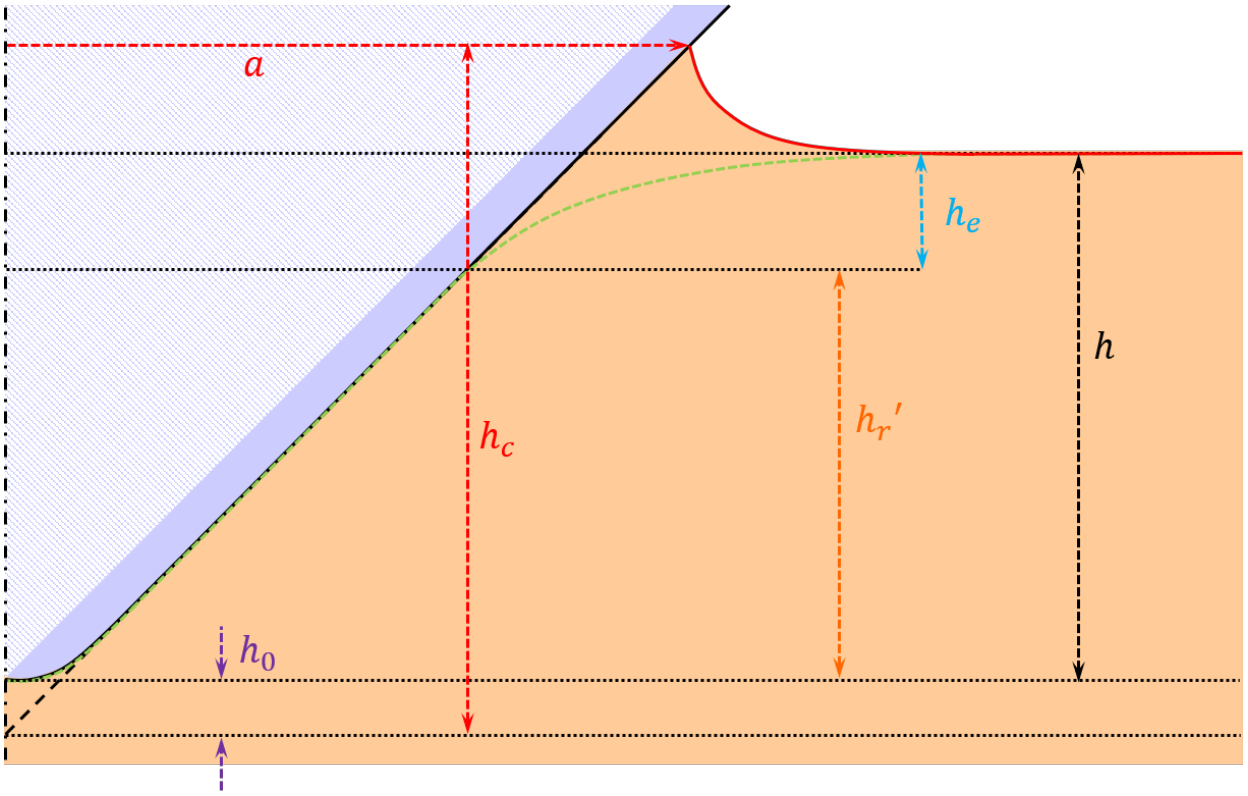

FIG. 10 Schematic representation of the contact geometry between a conical indenter and some material, defined in Loubet's model. h is the measured indentation depth, h_r' is the plastic depth, h_0 is the tip defect and h_c is the contact depth.

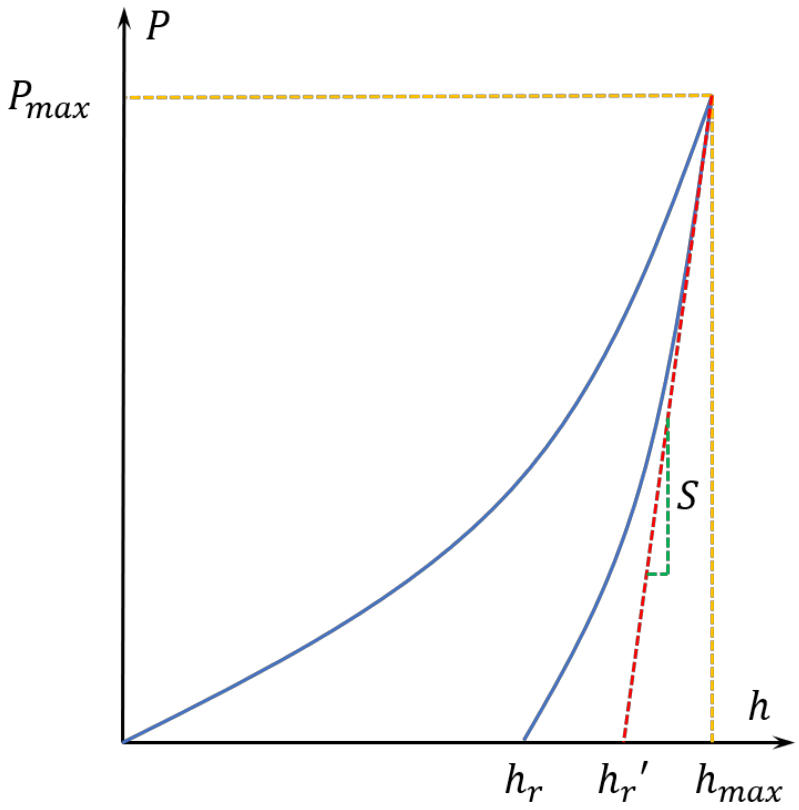

FIG. 11 Schematic load-displacement curve of a material. h_r is the persistent depth, and h_r' is the plastic depth.

3. Tip defect

When carrying out real experiments, the tip is never perfect. Therefore, the real contact area is underestimated if considering a perfect tip (see FIG. 10). The hatched purple area is a perfect tip contact area without defects. Because the real tip is slightly round, the purple zone should be added to the perfect contact area to obtain the real contact area. Therefore, to solve this issue, a tip defect term h_0 is added in the contact depth expression when calculating the tip contact.

$$h_r' = h - \frac{P}{S} + h_0 \qquad \text{Eq. 18}$$

This term could be easily determined when plotting stiffness against depth changes for a homogeneous material such as fused silica during calibration of the system with CSM measurements. For a perfect tip, this term should be $S(h) =$

bh. When there is a tip defect, the equation becomes $S(h) = b(h - h_0)$, and h_0 can be determined. Let us note that the obtained value of h_0 depends on the load frame stiffness determined by calibration.

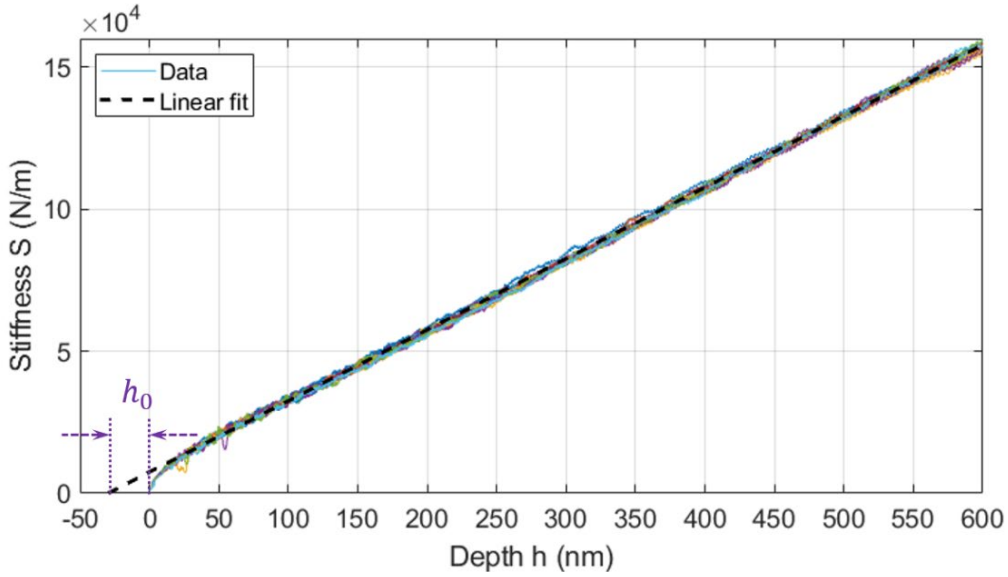

FIG. 12 Determination of the tip defect from the stiffness-displacement curve made on fused silica using CSM mode.

At low depth, the term h_0 allows us to be more precise in the calculation of the contact area. At large depths, the error between the ideal contact area and the real contact area becomes negligible.

4. Consideration of pile-up

Pile-up[46] can occur when performing indentation measurements. This effect increases the real contact area, so if not considered, the Young's modulus and hardness will be overestimated. Therefore, Loubet defined the contact depth using:

$$h_c = \alpha h_r' \qquad \text{Eq. 19}$$

with $\alpha = 1.2$ from experimental results[54,55]. This value was experimentally determined on gold by Bec et al.[55]. It was also validated theoretically for perfectly elastic materials[56] and numerically for perfectly plastic materials[56] in the case of a conical indenter. It is worth noting that when pile-up occurs, h_c could be higher than the maximum depth.

Looking to Eq. 19, the condition for sink-in is not forbidden. Loubet's model could also been applied to materials that presents sink-in. Guillonneau et al.[57] shows that Oliver and Pharr's model and Loubet's model give the same results on fused silica, which presents sink-in.

5. Independence to the load frame stiffness S_{LF}

Eq. 18 can be rewritten using u, the raw displacement of the tip instead of h, and the displacement corrected from the load frame stiffness when performing a nanoindentation experiment:

$$h_r' = u - \frac{P}{S_{LF}} - \frac{P}{S} + h_0 \qquad \text{Eq. 20}$$

Therefore:

$$\frac{1}{K} = \frac{1}{S} + \frac{1}{S_{LF}} \qquad \text{Eq. 21}$$

with K the global stiffness.

Therefore,

$$h_r' = u - \frac{P}{K} + h_0 \qquad \text{Eq. 22}$$

we can deduce from this expression that even if an error is made in the frame stiffness calculation, it will not change the plastic depth value because the elastic part of the displacement P/S (where S is not well calculated if S_{LF} is not well estimated) is removed from u to calculate h_r'. Therefore, with the use of Loubet's model, h_r', h_c and hardness H are independent of the load frame stiffness. This point is particularly interesting when performing experiments at low penetration depths for materials with high E/H ratios.

References

1. J. S. K.-L. Gibson, S. Schröders, C. Zehnder, and S. Korte-Kerzel: On extracting mechanical properties from nanoindentation at temperatures up to 1000 °C. *Extreme Mechanics Letters* **17**, 43 (2017).
2. B. D. Beake, A. J. Harris, J. Moghal, and D. E. J. Armstrong: Temperature dependence of strain rate sensitivity, indentation size effects and pile-up in polycrystalline tungsten from 25 to 950 °C. *Materials & Design* **156**, 278 (2018).
3. B. D. Beake and A. J. Harris: Nanomechanics to 1000 °C for high temperature mechanical properties of bulk materials and hard coatings. *Vacuum* **159**, 17 (2019).
4. C. Minnert, W. C. Oliver, and K. Durst: New ultra-high temperature nanoindentation system for operating at up to 1100 °C. *Materials & Design* **192**, 108727 (2020).
5. P. Baral, M. Laurent-Brocq, G. Guillonneau, J.-M. Bergheau, J.-L. Loubet, and G. Kermouche: In situ characterization of AA1050 recrystallization kinetics using high temperature nanoindentation testing. *Materials & Design* **152**, 22 (2018).
6. F. J. Humphreys and M. Hatherly: Recrystallization and Related Annealing Phenomena (Elsevier, 2004).
7. J. M. Wheeler, P. Brodard, and J. Michler: Elevated temperature, in situ indentation with calibrated contact temperatures. *Philosophical Magazine* **92**(25–27), 3128 (2012).
8. J. M. Wheeler and J. Michler: Indenter materials for high temperature nanoindentation. *Review of Scientific Instruments* **84**(10), 101301 (2013).
9. J. M. Wheeler: High temperature nanoindentation: The state of the art and future challenges. *Current Opinion in Solid State and Materials Science* **19**(6), 354 (2015).
10. N. M. Everitt, M. I. Davies, and J. F. Smith: High temperature nanoindentation – the importance of isothermal contact. *Philosophical Magazine* **91**(7–9), 1221 (2011).
11. J. M. Wheeler and J. Michler: Elevated temperature, nano-mechanical testing in situ in the scanning electron microscope. *Review of Scientific Instruments* **84**(4), 045103 (2013).
12. N. Bozzolo, S. Jacomet, and R. E. Logé: Fast in-situ annealing stage coupled with EBSD: A suitable tool to observe quick recrystallization mechanisms. *Materials Characterization* **70**, 28 (2012).
13. E. M. Lauridsen, S. Schmidt, S. F. Nielsen, L. Margulies, H. F. Poulsen, and D. J. Jensen: Non-destructive characterization of recrystallization kinetics using three-dimensional X-ray diffraction microscopy. *Scripta Materialia* **55**(1), 51 (2006).
14. F. Christien, M. T. F. Telling, K. S. Knight, and R. Le Gall: A method for the monitoring of metal recrystallization based on the in-situ measurement of the elastic energy release using neutron diffraction. *Review of Scientific Instruments* **86**(5), 053901 (2015).
15. E. M. Lauridsen, H. F. Poulsen, S. F. Nielsen, and D. Juul Jensen: Recrystallization kinetics of individual bulk grains in 90% cold-rolled aluminium. *Acta Materialia* **51**(15), 4423 (2003).
16. M. A. Z. Vasconcellos, R. P. Livi, and M. N. Baibich: Comparative study of isothermal and isochronal crystallisation of metallic glasses. *Journal of Physics F Metal Physics* **18**, 1343 (1988).
17. J. M. Pelletier, J. Perez, and J. L. Soubeyroux: Physical properties of bulk amorphous glasses: influence of physical aging and onset of crystallisation. *Journal of Non-Crystalline Solids* **274**(1), 301 (2000).
18. T. Fukami, K. Okabe, D. Okai, T. Yamasaki, T. Zhang, and A. Inoue: Crystal growth and time evolution in Zr–Al–Cu–Ni glassy metals in supercooled liquid. *Materials Science and Engineering: B* **111**(2), 189 (2004).
19. T. G. Nieh, C. Iwamoto, Y. Ikuhara, K. W. Lee, and Y. W. Chung: Comparative studies of crystallization of a bulk Zr–Al–Ti–Cu–Ni amorphous alloy. *Intermetallics* **12**(10), 1183 (2004).
20. Z. Zhang and J. Xie: Influence of relaxation and crystallization on micro-hardness and deformation of bulk metallic glass. *Materials Science and Engineering: A* **407**(1), 161 (2005).
21. M. Apreutesei, A. Billard, and P. Steyer: Crystallization and hardening of Zr-40at.% Cu thin film metallic glass: Effects of isothermal annealing. *Materials & Design* **86**, 555 (2015).
22. M. Idriss, F. Célarié, Y. Yokoyama, F. Tessier, and T. Rouxel: Evolution of the elastic modulus of Zr–Cu–Al BMGs during annealing treatment and crystallization: Role of Zr/Cu ratio. *Journal of Non-Crystalline Solids* **421**, 35 (2015).
23. Z. Wang: Influences of Sample Preparation on the Indentation Size Effect and Nanoindentation Pop-in on Nickel, 2012.
24. W. D. Nix and H. Gao: Size effects in crystalline : a law for strain gradient plasticity. *Journal of the Mechanics and Physics of Solids* **46**(3), 411 (1998).

25. O. Franke, J. C. Trenkle, and C. A. Schuh: Temperature dependence of the indentation size effect. *J. Mater. Res.* **25**(7), 1225 (2010).
26. R. D. Doherty, D. A. Hughes, F. J. Humphreys, J. J. Jonas, D. J. Jensen, M. E. Kassner, W. E. King, T. R. McNelley, H. J. McQueen, and A. D. Rollett: Current issues in recrystallization: a review. *Materials Science and Engineering A* 56 (1997).
27. B. N. Lucas and W. C. Oliver: Indentation power-law creep of high-purity indium. *Metall Mater Trans A* **30**(3), 601 (1999).
28. G. Kermouche, J. L. Loubet, and J. M. Bergheau: Cone indentation of time-dependent materials: The effects of the indentation strain rate. *Mechanics of Materials* **39**(1), 24 (2007).
29. A. H. W. Ngan, H. T. Wang, B. Tang, and K. Y. Sze: Correcting power-law viscoelastic effects in elastic modulus measurement using depth-sensing indentation. *International Journal of Solids and Structures* **42**(5–6), 1831 (2005).
30. W. C. Oliver and G. M. Pharr: An improved technique for determining hardness and elastic modulus using load and displacement sensing indentation experiments. *Journal of Materials Research* **7**(6), 1564 (1992).
31. J. L. Loubet, M. Bauer, A. Tonck, S. Bec, and B. Gauthier-Manuel: in *Mechanical Properties and Deformation Behavior of Materials Having Ultra-Fine Microstructures*, edited by M. Nastasi, D. M. Parkin, and H. Gleiter (Springer Netherlands, Dordrecht, 1993), pp. 429–447.
32. P. Baral, G. Kermouche, G. Guillonneau, G. Tiphene, J.-M. Bergheau, W. C. Oliver, and J.-L. Loubet: Indentation creep vs. indentation relaxation: A matter of strain rate definition? *Materials Science and Engineering: A* **781**, 139246 (2020).
33. G. Kermouche, J. L. Loubet, and J. M. Bergheau: Extraction of stress–strain curves of elastic–viscoplastic solids using conical/pyramidal indentation testing with application to polymers. *Mechanics of Materials* **40**(4–5), 271 (2008).
34. O. D. Sherby and P. E. Armstrong: Prediction of activation energies for creep and self-diffusion from hot hardness data. *Metall Mater Trans B* **2**(12), 3479 (1971).
35. J. W. Marx and J. M. Sivertsen: Temperature Dependence of the Elastic Moduli and Internal Friction of Silica and Glass. *Journal of Applied Physics* **24**(1), 81 (1953).
36. S. Spinner: Elastic Moduli of Glasses at Elevated Temperatures by a Dynamic Method. *J American Ceramic Society* **39**(3), 113 (1956).
37. S. Spinner and G. W. Cleek: Temperature Dependence of Young's Modulus of Vitreous Germania and Silica. *Journal of Applied Physics* **31**(8), 1407 (1960).
38. J. A. Bucaro and H. D. Dardy: High-temperature Brillouin scattering in fused quartz. *Journal of Applied Physics* **45**(12), 5324 (1974).
39. B. D. Beake: High-Temperature Nanoindentation Testing of Fused Silica and Other Materials. *Philosophical Magazine, Part A* **82**(10), 2179 (2002).
40. C. A. Schuh, C. E. Packard, and A. C. Lund: Nanoindentation and contact-mode imaging at high temperatures. *J. Mater. Res.* **21**(3), 725 (2006).
41. G. Simmons and H. Wang: Single Crystal Elastic Constants and Calculated Aggregate Properties: A Handbook (Cambridge, Mass., M.I.T. Press, 1971).
42. P. Ludwik: Über die Änderung der inneren Reibung der Metalle mit der Temperatur. *Zeitschrift für Physikalische Chemie* **91U**(1), 232 (1916).
43. J. M. Wheeler, V. Maier, K. Durst, M. Göken, and J. Michler: Activation parameters for deformation of ultrafine-grained aluminium as determined by indentation strain rate jumps at elevated temperature. *Materials Science and Engineering: A* **585**, 108 (2013).
44. P. S. Phani and W. C. Oliver: A direct comparison of high temperature nanoindentation creep and uniaxial creep measurements for commercial purity aluminum. *Acta Materialia* **111**, 31 (2016).
45. J. Shen, S. Yamasaki, K. Ikeda, S. Hata, and H. Nakashima: Low-Temperature Creep at Ultra-Low Strain Rates in Pure Aluminum Studied by a Helicoid Spring Specimen Technique. *Mater. Trans.* **52**(7), 1381 (2011).
46. D. Tabor: The hardness of solids. *RevPhysTech* **1**(3), 145 (1970).
47. D. Tumbajoy-Spinel, X. Maeder, G. Guillonneau, S. Sao-Joao, S. Descartes, J.-M. Bergheau, C. Langlade, J. Michler, and G. Kermouche: Microstructural and micromechanical investigations of surface strengthening mechanisms induced by repeated impacts on pure iron. *Materials & Design* **147**, 56 (2018).
48. M. Richou, A. Durif, M. Lenci, M. Mondon, M. Minissale, L. Gallais, G. Kermouche, and G. De Temmerman: Recrystallization at high temperature of two tungsten materials complying with the ITER specifications. *Journal of Nuclear Materials* **542**, 152418 (2020).

49. A. Leitner, V. Maier-Kiener, and D. Kiener: Dynamic nanoindentation testing: is there an influence on a material's hardness? *null* **5**(7), 486 (2017).
50. J. C. Trenkle, C. E. Packard, and C. A. Schuh: Hot nanoindentation in inert environments. *Review of Scientific Instruments* **81**(7), 073901 (2010).
51. F. Bachmann, R. Hielscher, and H. Schaeben: Grain detection from 2d and 3d EBSD data—Specification of the MTEX algorithm. *Ultramicroscopy* **111**(12), 1720 (2011).
52. F. Roudet: Propriétés mécaniques par indentation multi-échelles des matériaux bio-sourcés aux céramiques, 2015.
53. P. Sudharshan Phani and W. C. Oliver: A critical assessment of the effect of indentation spacing on the measurement of hardness and modulus using instrumented indentation testing. *Materials & Design* **164**, 107563 (2019).
54. K. Demmou: Nanoindentation, Viscoplasticité & Piézo-Mécanique de Films de Dithio-Phosphate de Zinc Triboformés, These, Ecole centrale de Lyon, 2007.
55. S. Bec, A. Tonck, J.-M. Georges, E. Georges, and J.-L. Loubet: Improvements in the indentation method with a surface force apparatus. *Philosophical Magazine A* **74**(5), 1061 (1996).
56. G. Guillonneau: Nouvelles Techniques de Nano-Indentation Pour Des Conditions Expérimentales Difficiles : Très Faibles Enfoncements, Surfaces Rugueuses, Température, These, Ecully, Ecole centrale de Lyon, 2012.
57. G. Guillonneau, J. M. Wheeler, J. Wehrs, L. Philippe, P. Baral, H. W. Höppel, M. Göken, and J. Michler: Determination of the true projected contact area by in situ indentation testing. *Journal of Materials Research* **34**(16), 2859 (2019).